Microstructure-Sensitive Probabilistic Fatigue at Notches in IN100

William D. Musinski and David L. McDowell
George W. Woodruff School of Mechanical Engineering
Georgia Institute of Technology
Atlanta, GA, 30332-0405, USA

Pratt & Whitney Progress Report for the Period 8/15/08-12/31/10
December 31, 2010

Introduction

Traditional fatigue analysis schemes used for geometries with stress gradient fields (such as notches) have required many experiments to determine the probability of fatigue failure. Due to the significant level of scatter in high cycle fatigue (HCF) phenomena, typically fatigue life data are fitted using many experimental data on the basis of an assumed distribution, often of Weibull or lognormal character. One engineering approach is to estimate notch effects on fatigue life via a notch root fatigue strength reduction factor, often alternatively called the fatigue notch factor, K_f, which is typically characterized experimentally. Experimental results are beneficial for life prediction for a given geometry and microstructure, but do not offer predictive insight into the underlying physical mechanisms that explain scatter, size effects, and gradient effects on fatigue damage. If the material is changed, the fatigue notch factor changes for a given geometry. Moreover, the fatigue notch factor concept inherently avoids an explicit definition of crack length at the point of fatigue crack initiation.

Recent probabilistic approaches for fatigue crack initiation [1-5] consider the probability of occurrence and competition among permissible fatigue failure mechanisms. For notched components, notch size effects influence the probability of occurrence of each failure mechanism. Experimentally performing parametric studies to distinguish each individual mechanism and probability of occurrence can be a very expensive and daunting task. Computational crystal plasticity models that characterize sensitivity to microstructure variability, notch size and gradient effects, and extrinsic defects (inclusions, FOD) can be used to qualitatively compare the relative contribution of each failure mechanism to the overall fatigue response of a component. The goal of this research is to develop approaches that combine computational crystal plasticity with nonlocal notch root plasticity and damage approaches for small crack formation in HCF, LCF, and mixed conditions, with applications to aircraft gas turbine engine materials. These approaches combine elements of crystal plasticity with new probabilistic methods for notch sensitivity based on computed slip distributions in the microstructure at the notch root.

Objectives of This Work

The purpose of this research is to extend microstructure-sensitive nonlocal fatigue modeling methodology previously conducted in the McDowell research group [6-8] to next generation notch root analysis for γ–γ′ Ni-base superalloys of relevance to aircraft gas turbine engine disk applications. Initial efforts within our group [9, 10] provided a basis for characterizing the probability of forming a crack at the scale of a grain as a function of the notch root radius relative to grain size in OFHC Cu. This research incorporates such effects as notch size effect, peak stress, stress gradient, and microstructure variability on formation and small fatigue crack growth through computational characterization of probability distributions of slip and small crack initiation processes, with application to Ni-base superalloys. These

distributions are informed by computational crystal plasticity simulations on realistic microstructures. In addition, this research is now exploring the relative effects of near surface inclusions and residual stresses on the fatigue of notched components with an eye towards improving minimum fatigue life design estimation techniques for notched components. With these methods in place we will be able to assess the potential for new alloys, heat treatments and surface treatments for notch fatigue resistance.

Project Milestones/Timeline

Start date: 8/15/08 - This project has been underway for 29 months.

- Task 1: Simulations of microstructure sensitive notch root response
- Task 2: Methods to assess notch sensitivity in terms of slip distribution and probability of crack initiation (crack formation plus small crack growth)
- Task 3: Integration with probabilistic notch root fatigue crack initiation estimation schemes and validation

Timeline:

- Task 1: Months 1-12 - Many different instantiations completed for various notch sizes and applied strain amplitudes.
- Task 2: Months 8-24 - Multiple formulations have been developed and exhibited [11, 12].
- Task 3: Months 20-36 - Deterministic crack formation and growth algorithms applied to simulated smooth specimen correlated well [11] with existing smooth specimen experimental strain life data [13, 14].

Approach

A fully three-dimensional computational polycrystal plasticity model [15] is used to simulate the complex deformation behavior of a supersolvus coarse grain (34 micron grain size [7]) IN100 Ni-base superalloy at $650°C$. This rate-dependent, microstructure-sensitive polycrystal plasticity model captures the first order effects on the macroscopic stress-strain response due to grain size and the size and volume fraction of secondary and tertiary γ' precipitates. These microstructure features all greatly affect the high temperature deformation mechanisms and fatigue response of nickel-base superalloys [16]. The polycrystal plasticity formulation is used in conjunction with deterministic crack formation and propagation techniques to assess the probability of failure of notched components. The probability of forming and propagating a crack from the grain scale to a transition crack length (where LEFM applicable) is approximated using shear-based fatigue indicator parameters (FIPs) computed within the uncracked notched specimen. This model for crack formation and early growth is calibrated to existing smooth specimen experiments. Cumulative distribution functions and probabilistic strain life functions are constructed for various notch root radii and remote strain amplitudes.

Progress

Modeling Stages of Fatigue Crack Formation and Growth

Three stages of fatigue crack formation and growth are modeled in the present investigation, including fatigue crack incubation, microstructurally small crack growth and linear elastic fracture mechanics (LEFM) crack growth. We characterize the Stage I, shear-dominated formation and growth of cracks through the use of the Fatemi-Socie (FS) parameter, $\Delta\Gamma$ [17]. This FIP takes into account the

plane of maximum cyclic plastic shear ($\Delta\gamma_{max}^{p^*}$) and the stress normal to this plane ($\sigma_n^{max^*}$) and takes the form

$$\Delta\Gamma = \frac{\Delta\gamma_{max}^{p^*}}{2}\left(1 + K^{'}\frac{\sigma_n^{max^*}}{\sigma_y}\right) \tag{1}$$

where $K^{'}$ is a constant that controls the effect of normal stress in fatigue crack formation and early growth, and σ_y is the cyclic yield strength. For consistency, the FIPs are averaged over a volume of scale 4 microns and are calculated over the third fatigue cycle for all simulation intantiations. In the present work, $K^{'} = 1.0$, which has been correlated to a wide variety of multiaxial loading histories for the fatigue life of IN718, a similar nickel-base superalloy [17].

In the present study, we consider crack incubation as the formation of a crack on the order of grain size. A simplified form of the Tanaka and Mura [18] crack incubation model was extended to microplasticity by Shenoy et al. [7] to estimate the incubation life for IN100 for a crack on the order of a grain size, i.e.,

$$N_{inc}\left(\frac{avg\left(\Delta\gamma_{max}^{p}\right)}{2}\right)^2 = \frac{\alpha_g}{d_{gr}}, \tag{2}$$

where $\alpha_g = 0.056\mu m$ -cycle [7].

Microstructurally small crack (MSC) growth depends strongly on the local microstructure and often displays an oscillatory behavior on a da/dN versus ΔK curve. Since there is no unique relationship between ΔK and da/dN, frequently a phenomenological mean value of the fluctuating small crack growth rate is used in small crack growth models. Here, a modified form of the MSC growth law proposed by Shenoy et al. [7] is used to estimate the number of cycles to propogate a crack within a notch root region incrementally from a_{j-1} to a_j

$$N_{prop,MSC}(a_{j-1} \rightarrow a_j) = \frac{\ln\left(\frac{a_j}{a_{j-1}}\right)}{A_{FS}\ \tau_y\ \Delta\Gamma_{ave}(a_{j-1}, a_j)}, \tag{3}$$

where a_{j-1} and a_j is the crack length at increment $j-1$ and j, respectively. Here, A_{FS} is a parameter fitted through experiments and τ_y is the critical resolved shear stress given by $\tau_y = \sigma_y / M$, where $M = 3.06$ is the Taylor factor for a randomly textured FCC polycrystalline aggregate [7]. It is noted here that the redistribution of stresses due to crack advance are not accounted for when estimating the FIP as a function of crack length. These crack growth stress redistribution effects will be incorporated in future work.

Linear elastic fracture mechanics is used to model the growth of a crack from a transition crack length, a_{L_D}, to a final crack size at failure (a_f) via the classical Paris-Erdogan law, $da/dN = C(\Delta K_{eff})^m$ [19]. Here, crack growth is considered to occur only for the tensile portion of the loading cycle, i.e., $\Delta K_{eff} = Y\ S_a\sqrt{\pi a}$ and the constants employed are estimated from fine grain IN100 long crack growth data [20] ($C = 2x10^{-7}$ and $m = 3.3$ for T= $650°C$, f= 0.33, R=0.05, and ΔK and da/dN are in units of MPa-$m^{1/2}$ and mm/cycle). It is noted that crack closure effects could be taken into account with such approaches as the Forman or Walker equations [19], but crack closure is not the

emphasis of the current study. The total life of a component is estimated as the superposition of each lives in each growth regime, i.e., $N_{total} = N_{inc} + N_{prop,MSC} + N_{prop,LEFM}$.

The deterministic crack formation and small crack growth formulations above were calibrated to experimental smooth specimen data (see Ref. [11] for detailed discussion). For the LCF regime, the coarse grain (CG) IN100 computational model was compared to the fatigue crack initiation experiments (Ref. Cowles et al. [13]) on a hot isostatic pressed (HIP) Astroloy, which has a similar grain size (30-70 microns [21]) as that of CG IN100 (34 microns). For the HCF to VHCF regimes, ultrasonic fatigue testing data on a PM Ni-base superalloy N18 at $450°C$ (ref. Figure 5 in [14]) was used for comparison.

Finite Element Simulation of Notched Components

The simulated double edge-notched component is decomposed into three regions: (1) the inner most notch root region imposes 3D polycrystal plasticity, (2) an intermediate region employs both macroscopic J2 cyclic plasticity theory and isotropic linear elasticity to minimize effects of discontinuity between the innermost polycrystal plasticity region and (3) the outermost isotropic linear elastic region. The dimensions of the polycrystal plasticity region are selected so that the distribution of microslip within the notch region is fully encapsulated for the applied loading conditions. Thus, there were no severe discontinuities in stress or strain response at the boundary of each region due to the differences in material modeling constitutive response. The model employs a finer mesh size of 4 microns in a localized region near the notch root (0.15ρ away from notch root) and contains a gradient mesh that gradually increases to the CG size (34) at the outside barrier of the polycrystal plasticity zone. The modeling strategy and input parameters for fatigue cycling of simulated double edge-notched specimens are summarized in Fig. 1. The height ($H = 10\rho$) and width ($W = 10\rho$) of the double edge-notched specimens depend on the notch root size (ρ). Simulations were completed for 20 different realizations for each permutation of input variables.

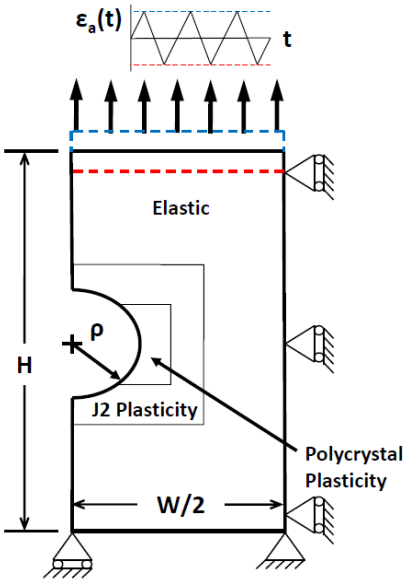

Variables	
Notch Radius – ρ (mm)	0.2, 0.4, 0.6, 0.8, 1.0
Strain Amplitude (ε_a / ε_y)	0.4, 0.5, 0.6
Constants	
Proportional Limit	$\varepsilon_y = 0.42\%$
Strain Rate	$\dot{\varepsilon} = 10^{-3}(s^{-1})$
R-Ratio (strain-controlled)	$R_\varepsilon = -1$

Figure 1: Modeling strategy for simulated double edge-notched specimens showing loading conditions, boundary conditions, and domain decomposition of material behavior.

The polycrystalline model is constructed using a spherical packing algorithm similar to that described in [22-24]. This algorithm offers more control over grain sizing as compared to a traditional random seed Voronoi tessellation, which results in a normal distribution. The values of $\mu = -0.1$ and $\sigma = 0.4$ were chosen for the target lognormal grain size distribution based on previous publications of fine grain IN100 grain size distributions [7, 15, 22, 25].

FIP-Based Transition Crack Length Approach

The transition crack length, L_d, is the distance at which a crack growing from a notch escapes the influence of the notch root stress concentration and is subject to treatment using conventional linear elastic fracture mechanics concepts. Here, the definition of transition crack length follows that of Smith and Miller [26] with a few exceptions. For a semi-circular notch, L_d is equal to 0.13 ρ [26]. For notches that are smaller than 0.5 mm, this may only constitute 1 or 2 grain diameters in the present CG IN100 microstructure. However, experiments have shown that crack growth data curves (da/dN vs. ΔK) for small cracks (EPFM) and long cracks (LEFM) merge at crack lengths on the order of 3-10 grain diameters [27]. Therefore, a transition crack length in which LEFM is applicable must constitute at least 3 grain diameters. This value may be arbitrary depending on the grain size. For example, experiments on a fine-grained (FG) IN100 microstructure have shown that the transition from oscillatory MSC to LEFM crack growth occurs at a crack length of about 100 microns [20], which is on the order of 20-25 grain diameters for the FG IN100 microstructure. This transition length of 100 microns coincides with a value of 3 grain diameters for the CG IN100 microstructure. Accordingly, the transition crack length values used in this study are

$$L_d = \begin{cases} 0.100, & \text{if } \rho \le 0.769 \\ 0.13 * \rho, & \text{if } \rho > 0.769 \end{cases} \tag{4}$$

Cumulative Distribution Function (CDF) Framework

Since the probability of formation of a crack on the order of transition crack length depends on the size of a preexisting crack (a_n) at a given number of cycles (N), we propose the form

$$CDF(S_a; L_d, N) = 1 - \exp\left[-\frac{\eta\, a_n}{L_d}\right] \tag{5}$$

The parameter $\eta = -\ln(0.5)$ provides normalization to the case for which the $CDF = 0.5$ when the crack reaches a transition crack length, L_d. The crack length a_n can be found by integrating the da/dN crack growth relationship. The CDF becomes

$$CDF(S_a; L_d, N) = 1 - \exp\left[-\frac{\eta}{L_d}\int_{N_{inc}}^{N} \frac{da}{dN} dN\right] \tag{6}$$

where the initial crack size (a_i) is on the order of the grain size. Through simulations the maximum value of FIP as a function of x-distance from the notch root, $\Delta\Gamma_{max}(x)$, is parameterized as an exponential decay function, i.e.,

$$\Delta\Gamma_{max}(x) = \Delta\Gamma_{max}(0) \exp\left(\frac{-\xi x}{L_d}\right) \tag{7}$$

Plotted in Fig. 2 is the distribution of $\Delta\Gamma_{max}(x)$ as a function of x distance from the notch root for different notch root sizes. Also plotted in this Figure is the best fit line (Eq. 7) for the data points located

within a distance, L_d, from the notch root. It is apparent from Fig. 2 that Eq. (7) works well for the desired regime ($x = 0$ to $x = L_d$). Additionally, there is a significant difference in FIP intensity between the five different notch root sizes. For larger notches, the maximum FIP is higher and the FIP field decays less rapidly as a function of distance from the notch root, which is indicative of notch size effects.

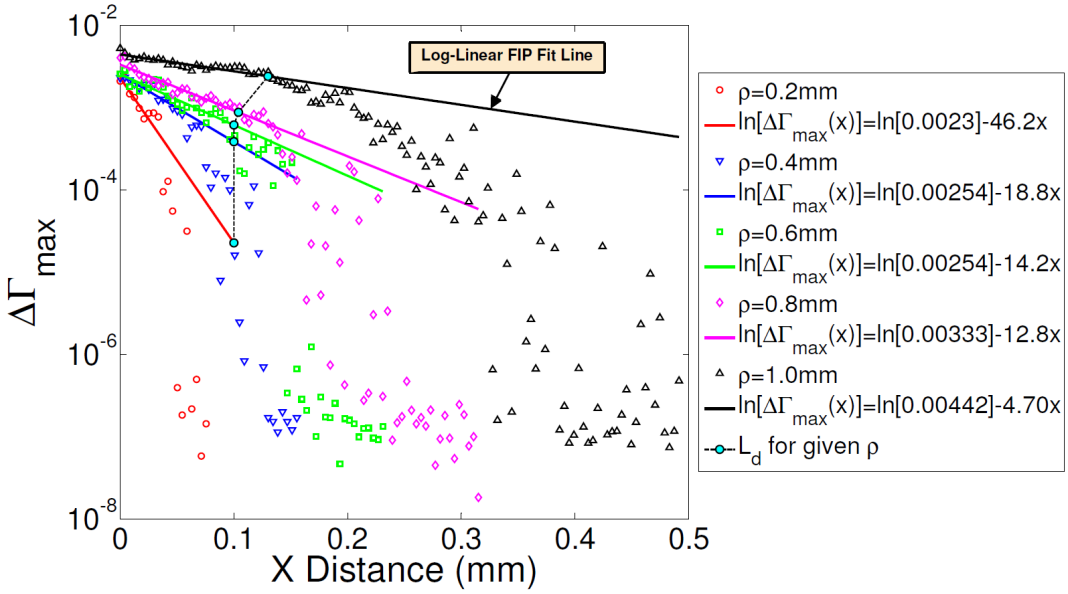

Figure 2: Maximum FIP distribution versus x-distance from notch root for 5 different notch root sizes, strain amplitude $\varepsilon_a = \varepsilon_y$.

The exponential decay function (Eq. 7) is used to determine the CDF function for each simulation run. First, the FIP distribution is divided into m discrete bins ($\Delta\Gamma_{max}(x_1)$, $\Delta\Gamma_{max}(x_2)$, …, $\Delta\Gamma_{max}(x_m)$). Next, the number of cycles to incrementally grow a crack from bin x_{j-1} to x_j is determined (Eq. 3) and used to construct a crack length, a_n, versus number of cycles N relationship. Finally, Eq. (5) is used to determine the CDF as a function of the number of cycles, the remotely applied stress amplitude, and the notch size.

Transition Crack Length Approach Results and Discussion

The grain structure, Von Mises uniaxial equivalent stress, and cumulative Von Mises effective plastic strain within the notch root region at maximum tensile load during the third fatigue cycle are shown in Fig. 3. The values of effective plastic strain below a value of $\bar{\varepsilon}^p = 10^{-7}$ were dropped from the contour plots to display the heterogeneity of plastic slip in the microstructure. As expected, the effective plastic strain is most significant at certain grain boundaries, which results from the incompatibility of deformation between grains of different orientation.

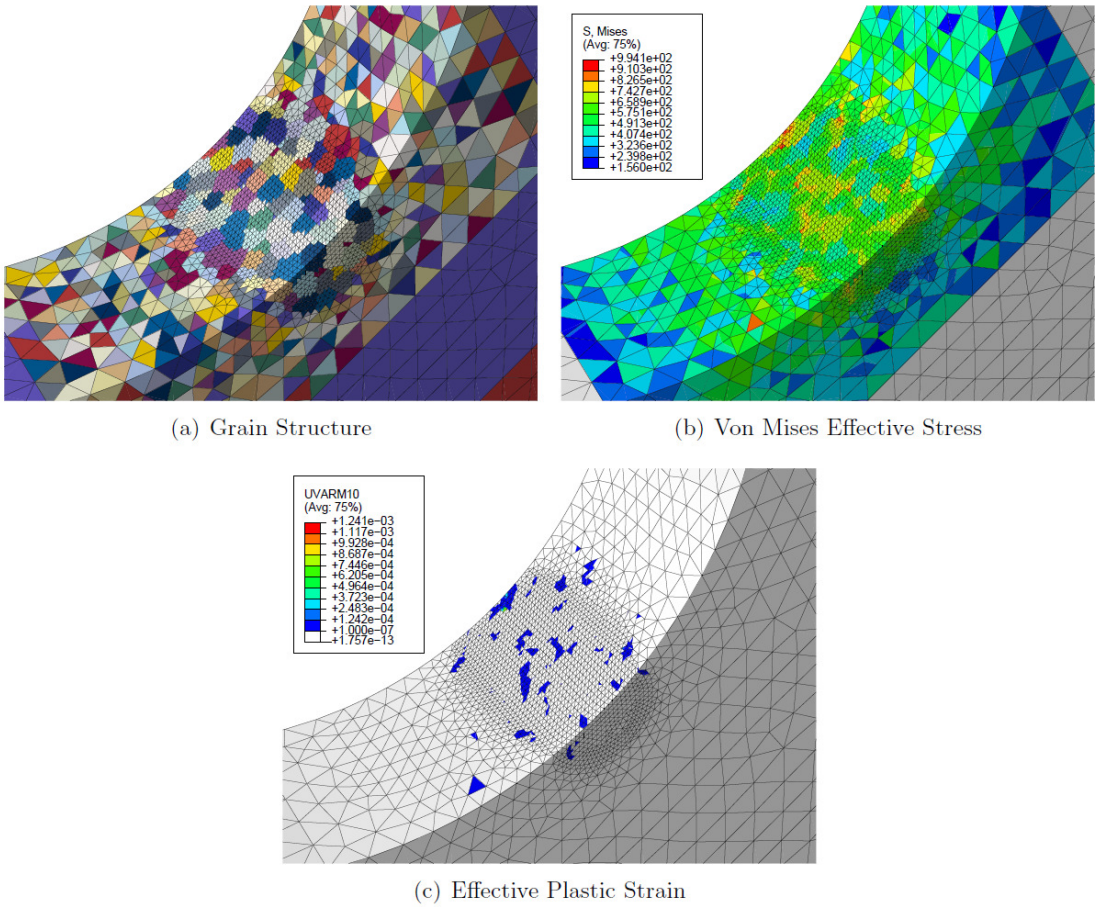

(a) Grain Structure

(b) Von Mises Effective Stress

(c) Effective Plastic Strain

Figure 3: Coarse Grain IN100 Contour Plots - $\rho = 0.6$, $\varepsilon_a = 0.6\varepsilon_y$.

Figure 4 displays the smooth and notched specimen strain-life data in addition to the smooth specimen experimental data [13, 14] that was used to calibrate the fatigue life prediction model [11]. Figure 4b compares the median data for all notch root sizes on a single plot. The median data point was used for comparison in this instance due to the large span of fatigue lives for a given strain amplitude. If the mean values were used, the behavior would be highly biased by the largest fatigue life value due to the logarithmic scale. As seen in the Figures, a notch effectively shifts the strain-life graph downward. It is interesting to note that the notch effect causes a significant drop in life for specimens loaded at a strain amplitude of $\varepsilon_a = 0.6\varepsilon_y$. For a smooth specimen loaded at this amplitude, a crack may not initiate even for a very high number of cycles (10^9 and beyond), if at all. This corresponds to the very high cycle fatigue range. On the other hand, a notched specimen at this strain amplitude exhibits a crack initiation life more consistent with the transition or HCF regime ($\sim 10^5 - 10^7$ cycles).

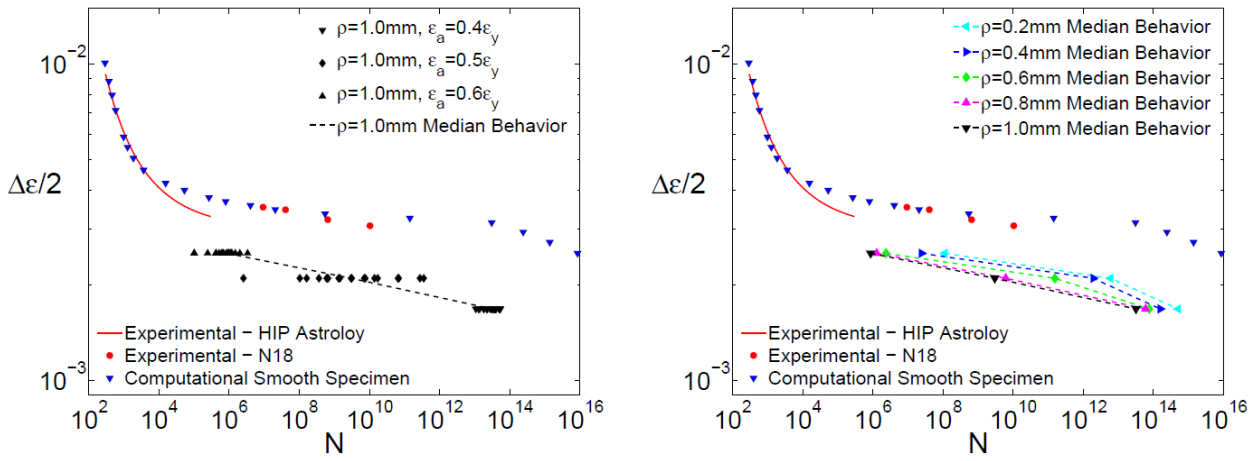

(a) $\rho = 1.0\,\text{mm}$. (b) Comparison of all notch root radii.

Figure 4: Comparison of CG IN100 smooth and notched computational strain life data versus HIP Astroloy [13] and N18 [14] smooth specimen experimental strain life data.

The results from the CDF framework are shown in Fig. 5. The benefit of using this approach is that the cumulative distribution function can be calculated for any number of cycles and any probability of failure. This approach can be applied to LCF, HCF and transition fatigue regimes to find the total component failure. Once the crack forms to the transition length, linear elastic fracture mechanics can be used to find the total component failure. This framework predicts that larger notch sizes will tend to fail before smaller notch sizes, which is consistent with general experimental trends.

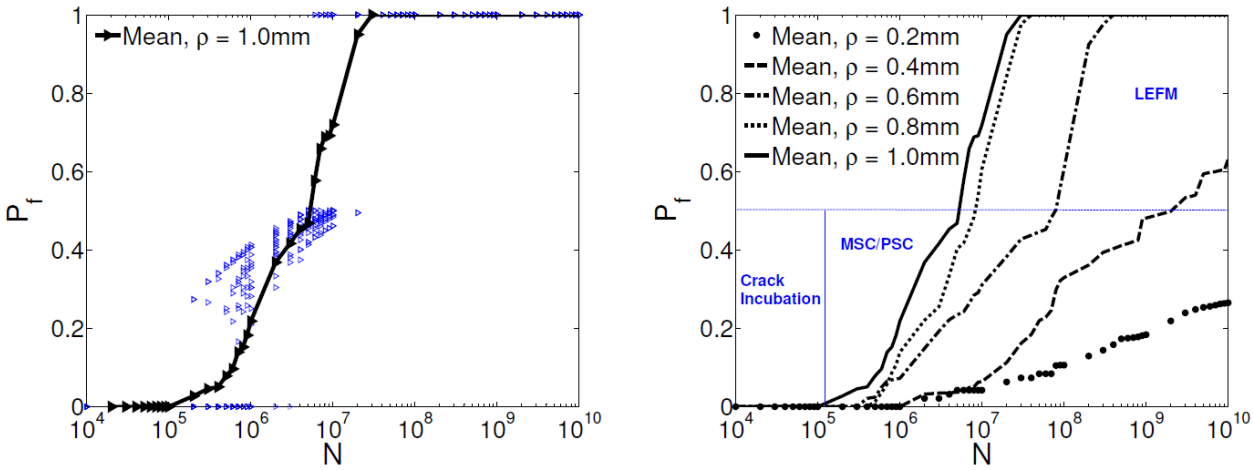

(a) $\rho = 1.0\,\text{mm}$. (b) Comparison of all notch root radii.

Figure 5: CG IN100 cumulative distribution function for various notch root radii ($\varepsilon_a = 0.6\,\varepsilon_y$, $\sigma_a = 450$, $R_\varepsilon = -1$, $T = 650°C$).

One limitation of the transition crack length approach is that it simplifies the complex nature of 3D crack formation, growth and nearest neighbor interactions into a simplified model that considers the FIP intensity over a characteristic transition length, similar to average stress models used to analyze notch

components. Another issue is that in reality stress redistributes during crack growth and the driving forces for crack propagation increase as the crack size increases, which is not considered in this particular formulation. For this reason, an approach to approximate the FIP redistribution due to crack advance is being developed for future work.

Recent and Ongoing Work

Incorporation of Residual Stresses

Surface compressive residual stresses are often introduced in a component to reduce the harmful effect of surface inclusions on fatigue life of a component. Compressive residual stresses help retard fatigue crack initiation [28] and early growth at near surface inclusions and shift the fatigue crack initiation sites from surface to subsurface locations [29, 30]. The helpful effects of surface residual stresses have been well documented in the literature [29-32]. Surface residual stresses can be applied via multiple techniques (shot/gravity peening, low plasticity burnishing, laser shock peening, etc.). The residual stress profile depends on the method of surface treatment (Ref. [33] for residual stress profile examples). Since the most commonly used technique in industry is shot peening, shot peening will be the focus of the initial residual stress study. However, an overly liberal amount of shot peening can induce extensive material damage and non-metallic inclusion cracking which can override the benefit of the shot peening process [34]. In addition, residual stress relaxation can occur through fatigue loading and by means of thermal recovery [35-37]. Thus, accurate fatigue life modeling of the effects of surface residual stresses due to shot peening should take into account plasticity-induced change in microstructure and load/temperature-induced residual stress relaxation. This section details the computional method used for introduction of residual stresses on the surface of a component.

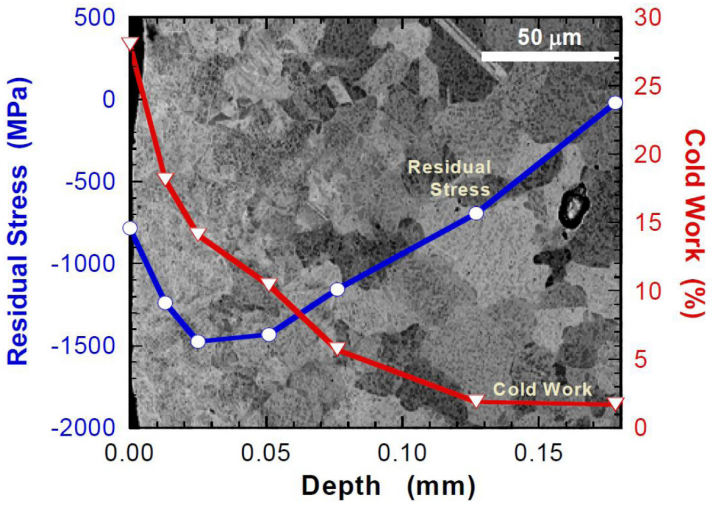

Figure 6: Residual stress and cold work profiles overlaid on supersolvus IN100 microstructure shot peened to 6A Almen intensity [35].

The computational methodology used here is similar to that developed in Prasannavenkatesan et al. [38]. During the shot peening process, equibiaxial compressive residual stresses are introduced near the surface due to constrained plastic deformation. Due to equilibrium, tensile stresses form within the subsurface of the material. To simulate the material stress state after the shot peening process, a simple computation model is used and calibrated to experimental residual stress XRD data as reported by Buchanan et al. [35]. In Buchanan et al. [35] they performed residual stress relaxation studies of a

supersolvus PM Ni-base superalloy IN100 with an average grain size of 25 microns that was shot peened to a Almen intensity of 6A. The resulting residual stress profile is overlaid on the shot peened microstructure in Fig. 6. As seen in Fig. 6, there is an intense amount of plasticity induced near the surface of the specimen.

The steps in applying the initial residual stress and calibration of residual stress relaxation are shown in Fig. 7 and can be summarized by:

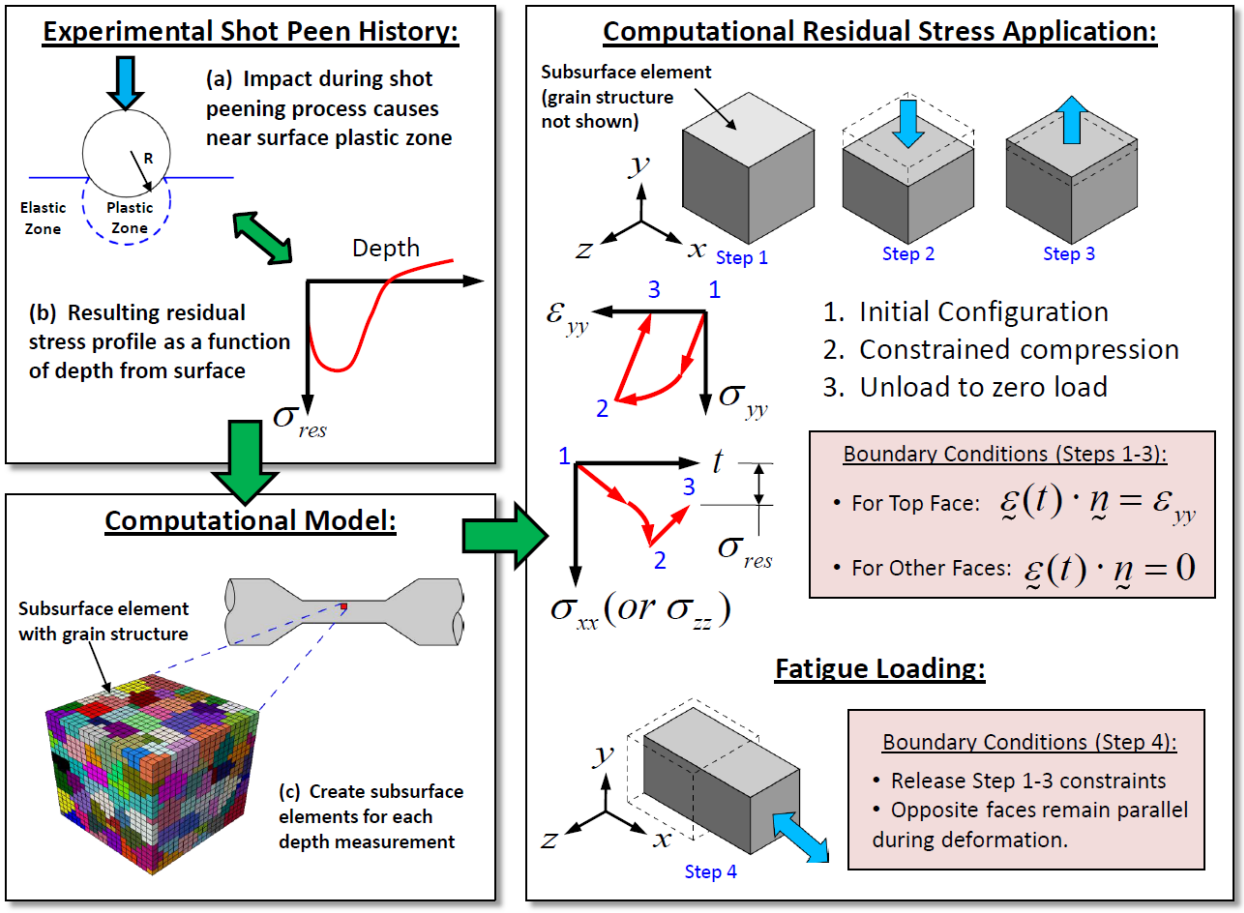

Figure 7: Methodology to simulate the mechanical shot peening process.

1. *Initial Configuration* - Using the experimental data, a number of subsurface elements (subvolume cube of material that contains $\sim$125 grains) are created to represent the material response at a given depth from the surface. Each depth is run separately to the strain-controlled maximum compression and unload levels that have been calibrated using the polycrystal plasticity model described above. These input strain values are further detailed in the next section.

2. *Constrained Compression* - During the shot peening process the material undergoes constrained compression perpendicular to the surface of the specimen. In each simulation, the top surface of the block of material (positive y-axis in Fig. 7) is considered to be parallel to the outward normal of the specimen surface. During the constrained compression step, each surface (except the top surface) of the block of the material is not allowed to move in the direction of the outward normal. Using these boundary conditions, the top surface is compressed using strain-controlled loading to the maximum

desired compressive strain.

3. *Constrained Unloading to Zero Load* - Using the same boundary conditions as in step 2, the block of material is unloaded in the y-direction to zero load ($\sigma_{yy} = 0$). This step represents the spring back of the material to zero load after the high velocity impact of the shot beads at the surface of the material.

4. *Fatigue Loading* - This step is used to calibrate the fatigue loading of the material in one of the principal residual stress directions and to estimate the residual stress relaxation due to subsequent loading. During this step, the boundary conditions of steps 2-3 are removed and an additional constraint is applied in which the opposite faces are required to remain parallel during deformation. Without this boundary condition, the material is free to completely dissipate any long range residual stresses within the bulk of the material through elastic hydrostatic unloading.

Residual Stress Imposition: Results and Discussion

Simulations of a single constrained compressive load/unload cycle were run at many different strain levels ($\varepsilon_{max} = m * \varepsilon_y$, where $m = \{1.0, 1.5, 2.0, \mathrm{L}, 14.5, 15.0\}$). Figure 8 shows the stress (σ_{yy}) versus strain (ε_{yy}) curves for some of these simulations. As evidenced in this figure, since this constrained compressive loading is highly hydrostatic, a larger amount of strain is required for initial yielding of the material ($\sim$ 2x the proportional limit, ε_y). This type of material behavior is prevalent in highly triaxial loading conditions such as the constrained loading conditions simulated here. Thus, there is a limit in the amount of maximum residual stress that can be applied to the computational model (cf. Fig. 9a).

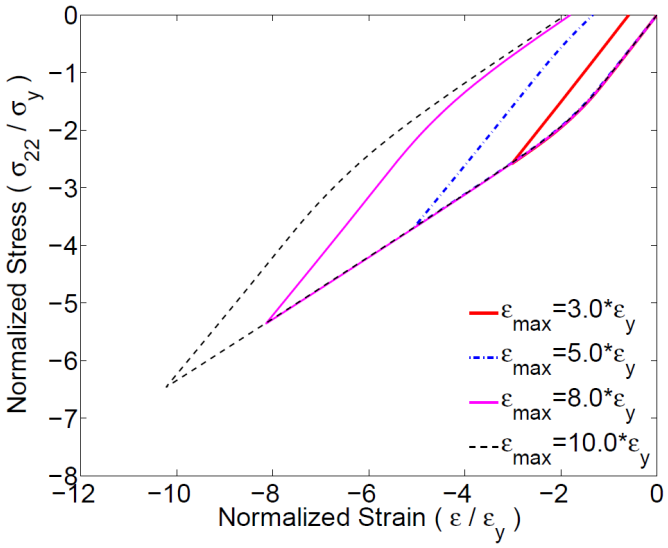

Figure 8: Stress strain curve for constrained compression of a CG IN100 smooth specimen.

There are two relationships required to calibrate the residual stress imposition model. First, the residual stress as a function of the maximum applied strain (maximum compressive strain) must be known. These results are shown in Fig. 9a. Second, the amount of unload strain (to $\sigma_{yy} = 0$) as a function of the maximum applied strain must be known. Figure 9b displays this relationship. As seen in both Figs. 9a and 9b, the normalization of the ordinate and abscissa axes results in a combined linear/sigmoidal type relationship. Therefore, these values were fit to a linear/sigmoidal relationship of

the form

$$y = Ax + B + \frac{C}{1+\exp\left[-D*(x-E)\right]} \tag{8}$$

where A, B, C, D and E are constants. These parameters were found using a Gauss-Newton [39] multi-parameter nonlinear regression scheme. The resulting optimized parameters are listed in each figure. Now that a simple relationship between the residual stress versus the required strain load/unload sequence is known, these input parameters can be used for subsequent fatigue loading and residual stress relaxation simulations as described in the next paragraph.

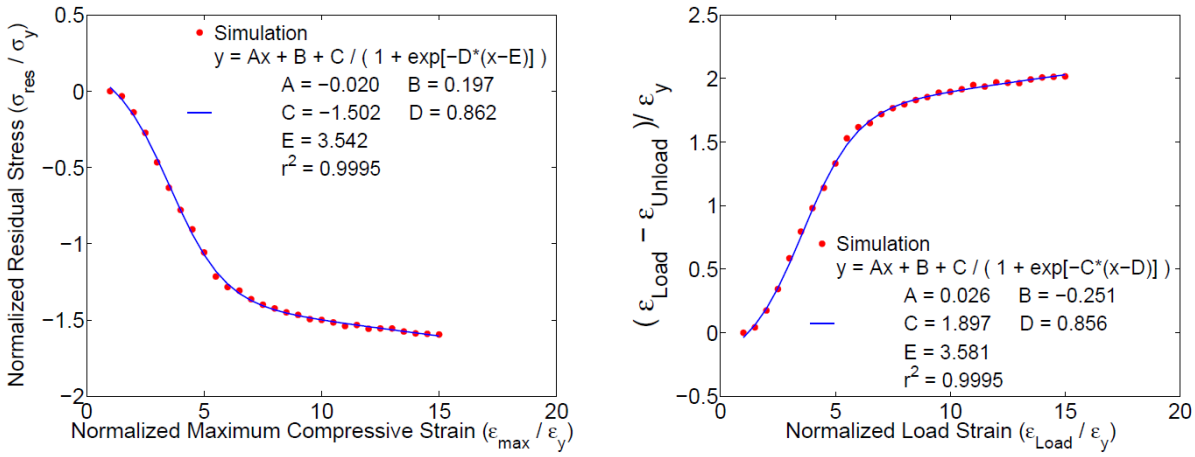

(a) Normalized residual stress versus maximum compressive strain applied.

(b) Unload strain required for unload to zero applied load.

Figure 9: Load and unload strain required for given residual stress application.

Next, multiple subvolumes of material are created to study the relaxation of residual stresses at different depth measurements. The calibrated load and unload strain requirements are shown for each depth measurement in Fig. 10. These values are used to prescribe displacement boundary conditions for imposing initial residual stresses as a function of subvolume depth. For the residual stress relaxation study, the computational data is compared to experimental data from [35]. In Ref. [35], they reported the amount of residual stress relaxation for a supersolvus coarse grain IN100 Ni-base superalloy after a single 900 load/unload cycle. Since the experimental supersolvus IN100 grain size ($d_{grn} = 25\mu m$) and monotonic yield strength ($\sigma_y = 900$ MPa) are slightly different than the computational model ($d_{grn} = 34\mu m$, $\sigma_y = 750$ MPa), the residual stresses are normalized by the yield strength for comparison. Also, the computational model was subjected to the load/unload cycle at its own monotonic yield strength ($\sigma_y = 750$ MPa). The results of the residual stress relaxation due to a single load/unload cycle are shown in Fig. 11. As seen from this figure, the computational model mimics the general shape of the experimental residual stress profile with a minor error. More investigation into the shape of the curve and better fitting will be pursued in future work. Also, the retention of the residual stresses during fatigue loading will also be considered.

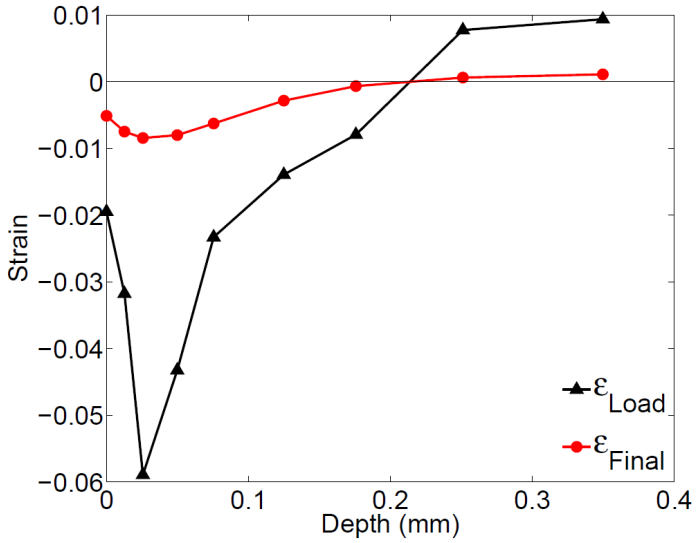

Figure 10: Load and final strain values required as a function of specimen depth to impose desired residual stress profile (cf. Fig. 6).

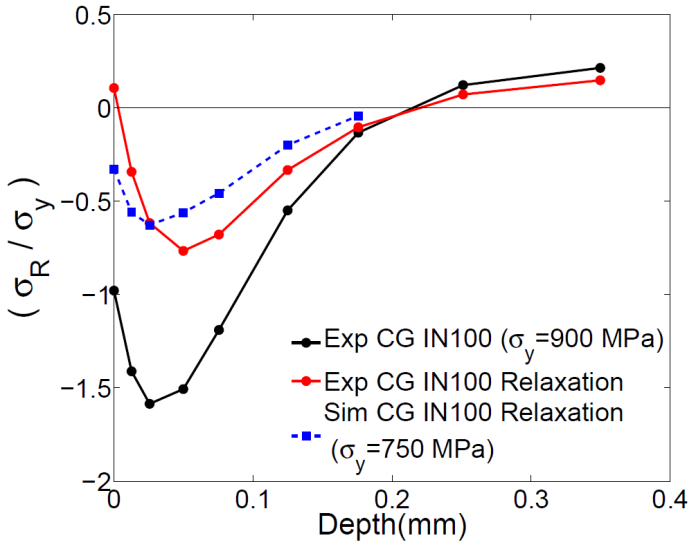

Figure 11: Comparison of residual stress relaxation due to single load/unload cycle for two supersolvus IN100 microstructures. Experimental data is from Buchanan et al. [35].

Considering Effect of Inclusions on Fatigue Life

One of the limiting factors of fatigue performance in PM Ni-base superalloys is the presence of nonmetallic inclusions (NMIs) that serve as crack initiation sites [40, 41]. These inclusions are often introduced to the molten metal, due to erosion or spalling of the crucible, tundish or nozzle, prior to the gas atomization process used to create the powder [5, 42]. Two types of ceramic inclusions are typically introduced during the powder atomization process [43]: a blocky, non-deforming Al_2O_3/MgO ceramics due to the breakage of the ceramic crucible and agglomerate and reactive inclusions originating from patching putties (Al_2O_3 with silicon traces). As the PM processing techniques improve, cleaner Ni-base

superalloys are being developed with reduced number densities of inclusions. However, proper probabilistic modeling of PM Ni-base superalloy components should take into account the probility of occurrence of a life-limiting NMI and the effect of the inclusion on the overall probability of failure. This approach should also consider the size effects associated with testing specimen-sized versus component-sized volume domains, since the statistically weakest ``defect'' size within a volume can change with the size of the volume [1, 42]. In the absence of a NMI, cracks can be initiated at pores located near the surface [44]. In Porter III et al. [44], they performed load control fatigue testing on two PM supersolvus Ni-base superalloys, Rene' 88DT and IN100, with average grain sizes of 30 and 25 microns, respectively. For Rene' 88DT, cracks initiated primarily at non-metallic inclusions (NMI) near the specimen surface. For IN100, life-limiting cracks initiated from pores 70% of the time and NMI the other 30%. Also, the cracks initiated mostly from the surface of the specimen (60%). Thus, the purpose of this investigation is to computationally determine the relative effect of inclusions and pores on the overall fatigue response and incorporate these effects in a proabilistic scheme to estimate the overall probability of failure of gas turbine engine components.

In this study, NMI and pore effects will be investigated through simulation of different size pores and NMIs. Based on probabilistic pore, NMI, and grain size distribution functions reported in literature [45], NMIs and pores near the surface will be simulated to determine the effect of these input parameters on fatigue variability. Since it is computationally infeasible to simulate every NMI and pore, we will simulate the most detrimental NMI/pore near the subsurface. The total probability of failure is then related to the probability of occurrence of each different failure mechanism. The overall approach for this study is summarized in Fig. 12.

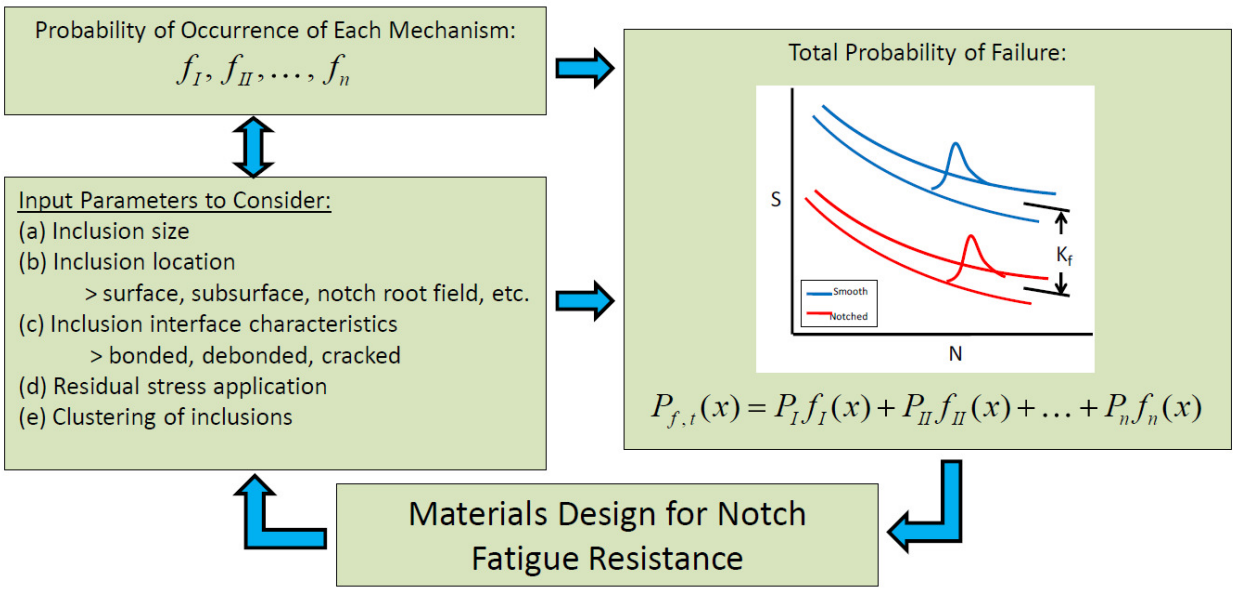

Figure 12: Probabilistic framework including effects of NMI and pores.

Stress Redistribution Due to Crack Advance

Finally, another direct extension of the current work is to consider the effect of stress redistribution with crack advance. As the crack growth advances, stress redistributes and the driving force for crack propagation increases as the crack size increases. This effect is not considered in the current probabilistic framework. One way to estimate the FIP redistribution due to crack growth is to run

simulations on both a cracked and uncracked specimen with the same polycrystalline microstructure within the crystal plasticity zone. The crack can be induced by eliminating elements within the notch root region of an uncracked notched specimen. Other approximation schemes could be developed to estimate the redistribution of FIP values. Another consideration that should be investigated is the effect of neighboring grains on the probability of crack advance. The conditional probability that a crack tip will retard, deflect or advance at the grain boundary depends strongly on the twist and tilt angle of the grain boundary [46]. As the crack grows larger, the crack can sample more grain boundaries and choose the path of least resistance. Crack advance is progressively less likely to get hung up at the grain boundary and the crack tip approaches a condition of similitude. The microstructure-sensitive modeling of this type of crack advance will be investigated in future work.

Summary and Future Work

The purpose of this work is to use computational crystal plasticity to explore the formation and growth of fatigue cracks in notched specimens to a transition crack length as a function of the notch size and applied strain amplitude. The strategy presented links notch root microstructure heterogeneity to scatter in fatigue response and notch size effects. A microstructure-sensitive computational polycrystal plasticity model was used to describe the distribution of shear-based fatigue indicator parameters within the notch root region. Deterministic crack formation and growth algorithms applied to a simulated smooth specimen correlated well with existing smooth specimen experimental strain-life data. This calibrated fatigue lifing model was then applied to specimens with various notch sizes. As expected, larger notch sizes displayed a larger notch size effect and fatigue knock down effect. A probabilistic framework based on microstructurally small crack growth to a transition crack length was used to characterize the cumulative probability of failure function. One benefit of this CDF formulation is that it can be determined for any probability of failure at any given number of cycles, which has implications in design for minimum fatigue life. Also, this probability density function and the notch gradient effect can be used in conjunction with probability of failure techniques where the probability of occurrence is considered for different failure mechanisms as described in [3, 4].

The techniques employed above can be used to improve the prediction of HCF and VHCF life of notched components employing materials with complex microstructures. The time required to experimentally determine the high cycle and very high cycle fatigue response of Ni-base superalloy components necessitates the use of computational and probabilistic strategies and experimental verification in parallel to improve the prediction of fatigue damage due to a notch. These techniques can be used in conjunction with experiments to help validate a new material or manufacturing technique to create a variant form of an existing material. The caveat with the probability approaches described in this paper is that more experimental data is needed to verify the computationally created failure probability distribution functions. Especially critical is the characterization of the tails of these distribution functions when designing for minimum life approaches. Thus, it is very important for carefully controlled experiments to substantiate microstructure-sensitive computational fatigue modeling of crack initiation and vice versa. Although the probabilistic framework developed above was applied to notched Ni-base superalloy specimens, the framework is general enough that it can be applied to any material system and can be used for multiple failure mechanisms.

In 2011, the techniques used to simulate residual stresses, inclusions and stress resdistribution due to crack advance will be further investigated, updated and implemented. Once the residual stress relaxation model is better calibrated to experiments, it will be used to model the notched components. In addition, simulations of debonded NMIs and pores in the near subsurface will be performed. The effects of neighboring grain disorientation will be also be investigated in future work. Other potential avenues for future research include the following:

- Considering more complex crack growth laws and the effect of stress redistribution ahead of the crack tip as the crack grows.
- Investigating effect of primary gamma prime spacing and clustering on crack growth enhancement in subsolvus IN100.
- Considering creep and thermomechanical fatigue effects.
- Incorporating effects of oxide formation on crack surfaces and ahead of cracks (irreversibility and crack path preference).

References

[1] A. Pineau. Superalloy discs durability and damage tolerance in relation to inclusions. Proceedings of a Conference on High Temperature Materials for Power Engineering 1990, 913-934, 1990.

[2] A. de Bussac. Prediction of the competition between surface and internal fatigue crack initiation in PM alloys. Fatigue Fract. Eng. Mater. Struct., 17(11):1319-1325, 1994.

[3] S. Jha, M. Caton, and J. Larsen. Mean vs. life-limiting fatigue behavior of a nickel-based superalloy. In Superalloys 2008, 565-572. Champion, PA, US: TMS, 2008.

[4] S. Deyber, F. Alexandre, J. Vaissaud, and A. Pineau. Probabilistic life of DA718 for aircraft engine disks. In Superalloys 718,625,706 and Derivatives., 97-110. Warrendale, PA, USA: TMS, 2006.

[5] A. de Bussac and J. Lautridou. A probabilistic model for prediction of LCF surface crack initiation in PM alloys. Fatigue Fract. Eng. Mater. Struct., 16(8):861-874, 1993.

[6] M. Shenoy, Y. Tjiptowidjojo, and D. McDowell. Microstructure-sensitive modeling of polycrystalline IN100. Int. J. Plasticity, 24(10):1694-1730, 2008.

[7] M. Shenoy, J. Zhang, and D. L. McDowell. Estimating fatigue sensitivity to polycrystalline Ni-base superalloy microstructures using a computational approach. Fatigue Fract. Eng. Mater. Struct., 30(10):889-904, 2007.

[8] Y. Tjiptowidjojo, C. Przybyla, M. Shenoy, and D. L. McDowell. Microstructure-sensitive notch root analysis for dwell fatigue in Ni-base superalloys. Int. J. Fatigue, 31(3):515-525, 2009.

[9] G. Owolabi, R. Prasannavenkatesan, and D. McDowell. Probabilistic framework for a microstructure-sensitive fatigue notch factor. Int. J. Fatigue, 32:1378-1388, 2010.

[10] G. M. Owolabi and D. L. McDowell. Microstructure-sensitive fatigue design for notched components. In ASME IMECE, vol. 11, 1-10. 2010.

[11] W. D. Musinski. Novel Methods for Microstructure-Sensitive Probabilistic Fatigue Notch Factor. Master's thesis, Georgia Institute of Technology, 2010.

[12] W. D. Musinski and D. L. McDowell. Microstructure-sensitive probabilistic fatigue modeling of

notched components. 2011. To be presented at TMS 2011.

[13] B. A. Cowles, J. R. Warren, and F. K. Haake. Evaluation of the cyclic behavior of aircraft turbine disk alloys, Part II. NASA CR-165123, 1980.

[14] C. Bathias and P. C. Paris. Gigacycle fatigue of metallic aircraft components. Int. J. Fatigue, 32(6):894-897, 2010.

[15] C. P. Przybyla and D. L. McDowell. Microstructure-sensitive extreme value probabilities for high cycle fatigue of Ni-base superalloy IN100. Int. J. Plasticity, 26(3):372-394, 2010.

[16] A. Pineau and S. D. Antolovich. High temperature fatigue of nickel-base superalloys - a review with special emphasis on deformation modes and oxidation. Engineering Failure Analysis, 16(8):2668-2697, 2009.

[17] A. Fatemi and D. Socie. A critical plane approach to multiaxial fatigue damage including out-of-phase loading. Fatigue Fract. Eng. Mater. Struct., 11(3):149-165, 1988.

[18] K. Tanaka and T. Mura. A dislocation model for fatigue crack initiation. J. Appl. Mech., 48(1):97-103, 1981.

[19] S. Suresh. Fatigue of Materials. Cambridge University Press, Cambridge, UK, 2nd edn., 1998.

[20] M. Caton and S. Jha. Small fatigue crack growth and failure mode transitions in a Ni-base superalloy at elevated temperature. Int. J. Fatigue, 32:1461-1472, 2010.

[21] J. Gayda and R. V. Miner. Fatigue crack initiation and propagation in several nickel-base superalloys at 650oc. Int. J. Fatigue, 5(3):135-143, 1983.

[22] M. Groeber, S. Ghosh, M. D. Uchic, and D. M. Dimiduk. A framework for automated analysis and simulation of 3D polycrystalline microstructures.: Part 1: Statistical characterization. Acta Mater., 56(6):1257-1273, 2008.

[23] M. Groeber, S. Ghosh, M. D. Uchic, and D. M. Dimiduk. A framework for automated analysis and simulation of 3D polycrystalline microstructures. part 2: Synthetic structure generation. Acta Mater., 56(6):1274-1287, 2008.

[24] C. P. Przybyla and D. L. McDowell. Simulation-based extreme value marked correlations in fatigue of advanced engineering alloys. Procedia Engineering, 2(1):1045-1056, 2010.

[25] A. M. Wusatowska-Sarnek, G. Ghosh, G. B. Olson, M. J. Blackburn, and M. Aindow. Characterization of the microstructure and phase equilibria calculations for the powder metallurgy superalloy IN100. J. Mater. Res., 18(11):2653-2663, 2003.

[26] R. A. Smith and K. J. Miller. Fatigue cracks at notches. Int. J. Mech. Sci., 19(1):11-22, 1977.

[27] D. L. McDowell. Basic issues in the mechanics of high cycle metal fatigue. Int. J. Fract., 80(2-3):103-145, 1996.

[28] R. John, J. M. Larsen, D. J. Buchanan, and N. E. Ashbaugh. Incorporating residual stresses in life prediction of turbine engine disks. In RTO AVT Symposium, Manchester, UK, Oct. 8-11. 2001.

[29] K. Shiozawa and L. Lu. Very high-cycle fatigue behaviour of shot-peened high-carbon-chromium bearing steel. Fatigue Fract. Eng. Mater. Struct., 25(8-9):813-822, 2002.

[30] M. Larsson, A. Melander, R. Blom, and S. Preston. Effects of shot peening on bending fatigue strength of spring steel SS 2090. Mater. Sci. Technol., 7:998-1004, 1991.

[31] C. S. Montross, T. Wei, L. Ye, G. Clark, and Y. Mai. Laser shock processing and its effects on microstructure and properties of metal alloys: a review. Int. J. Fatigue, 24(10):1021-1036, 2002.

[32] P. Peyre, R. Fabbro, P. Merrien, and H. P. Lieurade. Laser shock processing of aluminium alloys. application to high cycle fatigue behaviour. Mater. Sci. Eng., A, 210(1-2):102-113, 1996.

[33] P. Prevey. The effect of cold work on the thermal stability of residual compression in surface enhanced IN718. In 20th ASM Materials Solutions Conf., St. Louis, MO, Oct. 1012., vol. 1, 426-434. 2000.

[34] R. Barrie, T. Gabb, J. Telesman, P. Kantzos, A. Prescenzi, T. Biles, and P. Bonacuse. Effectiveness of shot peening in suppressing fatigue cracking at non-metallic inclusions in udimet 720. Mater. Sci. Eng., A, 474(1-2):71-81, 2008.

[35] D. J. Buchanan, R. John, R. A. Brockman, and A. H. Rosenberger. A coupled creep plasticity model for residual stress relaxation of a shot peened nickel-base superalloy. In Superalloys 2008, 965-974. TMS, 2008.

[36] M. Khadhraoui, W. Cao, L. Castex, Gu, and J. Y. dou. Experimental investigations and modelling of relaxation behaviour of shot peening residual stresses at high temperature for nickel base superalloys. Mater. Sci. Technol., 13:360-367, 1997.

[37] W. Cao, M. Khadhraoui, B. Brenier, Gu, J. Y. dou, and L. Castex. Thermomechanical relaxation of residual stress in shot peened nickel base superalloy. Mater. Sci. Technol., 10:947-954, 1994.

[38] R. Prasannavenkatesan, J. Zhang, D. L. McDowell, G. B. Olson, and H. Jou. 3D modeling of subsurface fatigue crack nucleation potency of primary inclusions in heat treated and shot peened martensitic gear steels. Int. J. Fatigue, 31(7):1176-1189, 2009.

[39] S. C. Chapra and R. P. Canale. Numerical Methods for Engineers. McGraw-Hill, New York, NY, 2002.

[40] J. Hyzak and I. Bernstein. Effect of defects on the fatigue crack initiation process in two P/M superalloys - 1. Fatigue origins. Metall. Mater. Trans. A, 13 A(1):33-43, 1982.

[41] J. Hyzak and I. Bernstein. Effect of defects on the fatigue crack initiation process in two P/M superalloys - 2. Surface-subsurface transition. Metall. Mater. Trans. A, 13 A(1):45-52, 1982.

[42] R. C. Reed. The Superalloys; Fundamentals and Applications. Cambridge University Press, Cambridge, UK, 2006.

[43] A. Wusatowska-Sarnek, P. Bhowal, D. Gynther, and R. Montero. Effect of non-metallic inclusions on notched low cycle fatigue in P/M IN100 nickel-base superalloy. In 5th International Conference on Processing and Manufacturing of Advanced Materials, vol. 539-543 of Materials Science Forum, 2960-2965. Trans Tech Publications Ltd, Stafa-Zuerich, CH-8712, Switzerland, 2007.

[44] W. Porter III, K. Li, M. Caton, S. Jha, B. Bartha, and J. Larsen. Microstructural conditions contributing to fatigue variability in P/M nickel-base superalloys. In 11th International Symposium on Superalloys, Superalloys 2008, September 14, 2008 - September 18, 2008, Proceedings of the International Symposium on Superalloys, 541-548. Champion, PA: The Minerals, Metals and Materials Society, 2008.

[45] S. Jha, M. Caton, and J. Larsen. The mean vs life-limiting fatigue response of a Ni-base superalloy, part I: mechanisms. AFRL-RX-WP-TP-2009-4210, 2008.

[46] T. Zhai, A. J. Wilkinson, and J. W. Martin. A crystallographic mechanism for fatigue crack propagation through grain boundaries. Acta Mater., 48(20):4917-4927, 2000.